Applied Thermal Engineering 160 (2019) 114027

Contents lists available at ScienceDirect

Applied Thermal Engineering

journal homepage: www.elsevier.com/locate/apthermeng

Research Paper

LBM simulates the effect of sole nucleate site geometry on pool boiling

Ping Zhou[a], Zhichun Liu[a,*], Wei Liu[a], Xili Duan[b]

[a] School of Energy and Power Engineering, Huazhong University of Science and Technology, 430074 Wuhan, China
[b] Faculty of Engineering and Applied Science, Memorial University of Newfoundland, St. John's, NL A1B 3X5, Canada

HIGHLIGHTS

- LBM is used to simulate nucleate boiling for four different cavity structured surfaces.
- Circular and trapezoidal cavity structured surfaces are easier for onset of boiling.
- Heat transfer performance on different surfaces are analyzed.
- The main heat transfer mechanism in nucleate boiling process is the microlayer evaporation.

ARTICLE INFO

Keywords:
Lattice Boltzmann method
Square cavity
Circular cavity
Trapezoidal cavity
Inverted trapezoidal cavity

ABSTRACT

A two-particle distribution functions lattice Boltzmann method is selected to simulate periodic bubble nucleation, growth and departure from four different boiling nucleate cavity structured surfaces: square, circular, trapezoidal, and inverted trapezoidal. The effects of different structured nucleate site on bubble growth and departure are investigated in this paper. Fluid hydrodynamic and thermodynamic are characterized by the density distribution function and the temperature distribution function respectively. Pseudo-potential model and Peng-Robinson equations of state are selected in our simulations. Constant temperature boundary condition is applied to the bottom solid. It is found that at the four different structure cavity surfaces, at the given superheat temperature 0.96Tc, all the cavities are activated as boiling nucleate sites, but the onset boiling time on circular and trapezoidal cavity structure surfaces are shorter than on the other two surfaces. The temperature distribution pictures and the heat flux variation pictures for the four different cavity surfaces are given to analyze the heat transfer performance on different surfaces. The temperature distributions have obvious different on different cavity geometry surfaces in the bubble nucleation process. The heat flux distribution pictures show that the main heat transfer mechanism in nuclear boiling process is the microlayer evaporation.

1. Introduction

Boiling heat transfer has a widespread application no matter in the industrial about energy, power, chemical, refrigeration, machining and material or in the technosphere about spaceflight, rocket and nuclear energy [1,2]. For nearly one century, scholars from various countries have been doing a lot of experiments to study the boiling phenomenon, which includes the formation, growth, departure and rise of bubbles, or the mechanism and the correlation of boiling heat transfer and so on. So far, all these studies have achieved great progresses, and it can be used to solve some engineering problems for the equipment better design and operation. Despite this, the studies about boiling phenomenon are still in the development stage because of the variability and complexity, such as the uncertainty of the liquid-vapor interface, the high non-linearity of governing equations and so on. Up to now, the studies about the nucleate boiling are mainly focused on three aspects, means the pool boiling heat transfer mechanisms, the bubble dynamics and how to increase the critical heat flux (CHF) and boiling heat transfer coefficient (HTC).

Between the year of 1931 and 1936, Jakob et al. did a series experiments about the boiling heat transfer phenomenon [3,4]. They put forward some instructive opinions, for example, the high heat transfer rates in nucleate boiling on the one hand is attributed to the bubbles' agitation to the liquid, on the other hand, is also induced by liquid jets flowing in between rising columns and impinging on the heating surface. Since then, pool boiling heat transfer mechanism has been studied by many researchers as an efficient heat transfer means. Enhanced convection, transient conduction, microlayer evaporation, and contact line heat transfer have all been proposed as heat transfer mechanisms on the boiling process [5]. Because of the complex of boiling process,

* Corresponding author.
E-mail addresses: zcliu@hust.edu.cn (Z. Liu), w_liu@hust.edu.cn (W. Liu).

https://doi.org/10.1016/j.applthermaleng.2019.114027
Received 20 January 2019; Received in revised form 19 May 2019; Accepted 26 June 2019
Available online 02 July 2019

Nomenclature

a	constant in P-R equation of state
b	constant in P-R equation of state
c	lattice speed (m/s)
c_p	specific heat at constant pressure (J Kg^{-1} K^{-1})
$c_{p,l}$	specific heat of the liquid at constant pressure (J Kg^{-1} K^{-1})
c_s	lattice sound speed (m/s)
c_v	specific heat at constant volume (J Kg^{-1} K^{-1})
$\vec{e}$	lattice velocity vector (m/s)
$f_i(\vec{x}, t)$	density distribution function (Kg/m^3)
$\vec{F}$	force (N)
$\vec{F_g}$	gravitational force (N)
$\vec{F_{int}}$	interparticle interaction force (N)
$\vec{F_s}$	fluid-solid interaction force (N)
$g_i(\vec{x}, t)$	temperature distribution function (K)
g	gravitational acceleration (m/s^2)
g_s	fluid-solid interaction strength coefficient
h_{fg}	specific latent heat (J/Kg)
k	thermal conductivity (W m^{-1} K^{-1})
l_o	capillary length (m)
p	pressure (pa)
Pr	Prandtl number
$q(t)$	space-averaged heat flux (W/m^2)
$q^{'}(t)$	space-averaged dimensionless heat flux
R	constant in P-R equation of state
t	time (s)
t^*	dimensionless time
t_o	characteristic time (s)
T	temperature (K)
u_o	characteristic velocity (m/s)
$\vec{u}$, $\vec{U}$	velocity vector (m/s)
v	specific volume (m^3/Kg)
Nu	Nusselt number
x	co-ordinates (m)
y	co-ordinates (m)

Greek symbol

β	weighting factor of the interparticle interaction force
ρ	density (Kg/m^3)
Ψ	effective mass ($Kg^{1/2}$ $m^{-1/2}$ s^{-1})
ω	acentric factor in P-R equation of state
ω_i	weighting coefficients in D3Q19 lattice
Φ	source term (K/s)
γ	thermal mass ratio of the solid and the fluid
τ	relaxation time
σ	surface tension (N/m)
δ	lattice spacing (m)
ν	kinematic viscosity (m^2/s)
μ	dynamic viscosity (Pa·s)
α	thermal diffusivity (m^2/s)
∇	the gradient operator

Subscripts or Superscripts

c	critical
eq	equilibrium
f	fluid
l	liquid
r	receding
s	solid
sat	saturation
v	vapor
w	wall
x	co-ordinates
y	co-ordinates

there are some different models that account for the bubble heat transfer and different model has different emphasis. Transient conduction model is proposed by Mikic and Rohsenhow in 1969 [6]. They think the main mechanism of heat transfer in nucleate boiling is transient heat conduction to the superheated layer around boiling sites associated with bubble departure [6]. The second important model is the microlayer heat transfer model which suggests that growing bubble could trap a thin layer of liquid at the wall, and this thin layer can transfer substantial amounts of heat [5]. In the year of 1994, Stephan and Hammer proposed a new model to calculate heat transfer coefficients in nucleate boiling [7]. In this model, they think the evaporation of a thin liquid meniscus at the three-phase contact line is the main way of heat transfer.

The rate of boiling heat transfer is affected by various bubble dynamics parameters such as bubble growth time and waiting time, departure size and shape, departure frequency and so on. So bubble dynamics are also important parts of pool boiling heat transfer studies. These dynamics parameters have been found to be affected by heater size, gravity, superheat, surface structure. Deng et al. did an experimental study of the heater size effect on micro boiling, in which they found that there existed a critical heater size: single spherical bubble generation with heater's feature size less than 10 μm; oblate vapor blanket on the heater surface with the size larger than 10 μm [8]. Qiu et al. by making the artificial cavity in the polished silicon wafer, they did an experimental study of dynamics of single vapor bubbles during nucleate boiling in the low-gravity conditions. They found that there are larger bubble liftoff diameters and longer bubble growth periods than those at Earth normal gravity [9]. Buchholz et al. did a study of local heat transfer mechanisms along the entire boiling curve [10]. Their results showed that different superheat corresponds to different boiling mechanism. Thiagarajan et al. performed experiments on microporous copper surfaces and plain surfaces [11]. They found that on the microporous surfaces, 70% of the total heat was contributed by the evaporative component, while it is equal to quenching components on the plain surfaces, thus confirming that microporous coating enhances nucleate boiling transfer because of the higher active nucleation site density. Also, the microporous surfaces showed a significantly lower boiling incipience temperature due to the presence of cavities.

How to increase the HTC and CHF is a hot issue in boiling heat transfer aspect. Up to now, there are two main passive technologies that used to enhance pool boiling heat transfer. One is the use of new working fluid, such as mixture fluid [12,13], ferrofluid [14,15], nanofluids [16,17] and so on. The other is the surface modification technologies [18], include the nano-coated surface [19] or the micro- nano-structured surface [20,21]. In general, there are some characteristics for the modified surfaces on the pool boiling process: increase retentate gas in the micro- or nano-structure; increase nuclear boiling site; increase surface area; increase capillary; increase bubble departure frequency; change the surface wettability; decrease the onset boiling temperature. So these modified surfaces have proved to enhance HTC and CHF compared with bare surface [22–24].

Various experiments studies have been performed for the analysis of pool boiling mechanism and for the enhancement of heat transfer. But the experiments are always limited by some technical means such as micro- or nano-scale observation and operation. So it is necessary to develop some numerical methods in pool boiling simulation. Lattice

Boltzmann method (LBM) is one of the most comprehensive numerical methods in micro- or nano-scale. Ryu et al. used free energy based multiphase LBM to directly simulate nucleate pool boiling [25]. In their simulation, the effects of gravity force, surface tension, contact angle and wall superheat on bubble departure diameter are investigated. Also, the vapor bubble shape and temperature fields are compared to the experimental measurements. Sun et al. used a hybrid LBM to study nucleate boiling flows on a horizontal plate, in which they think the transient micro-convection is the main heat transfer means in the nucleate boiling [26]. Begmohammadi et al. utilized the LBM of Lee, which is applicable to high density ratio of liquid-vapor phenomena, to simulate bubble periodic growth on and departure from a superheated wall [27], in which the effect of density ratio up to 1000 on the frequency of bubble release was investigated. Sadeghi et al. extended the modified Lee model and a three-dimensional LBM is proposed to simulate pool boiling with high-density ratios on horizontal superheated walls [28]. Shan-Chen pseudopotential LB approach is very popular in the multiphase LBM community due to its conceptual simplicity and computational efficiency. Li et al. [29] and Gong et al. [30] have used pseudopotential LB model successfully simulating boiling curve. In this paper, we utilized Gong and Cheng's LB model to simulate nuclear boiling on different cavity geometry surfaces. Fang et al. have used a 2D multiple-relaxation-time pseudopotential LBM combined with the modified thermal LBM to simulate bubble growth process on a heated plate [31]. In the paper, they simulated different width of the rectangular cavity and they think there exists an optimal width making the best heat transfer performance of surfaces. Also, they simulated different geometry cavity in the same aperture radius, and they found circle cavity has the best heat transfer performance. Different from their work, in this paper, we simulated four different geometry cavity surfaces which nearly have the same area but different aperture radius. The bubble nucleation, growth and departure from the surfaces and corresponding heat transfer performances on different surfaces are analyzed.

2. Numerical method

In this paper, we use a liquid-vapor phase-change lattice Boltzmann method, which is proposed by Gong and Cheng [32] in 2012, to simulate different cavity geometry surfaces nucleate boiling phenomenon. In this model, Shan and Chen pseudo potential LB is selected and in their original pseudo potential LB model, the Bhatnagar–Gross–Krook (BGK) collision operator was employed. We also choose exact difference method (EDM) in the forcing scheme, which is verified more stable in pseudo potential LB. A brief introduction about liquid-vapor phase-change lattice Boltzmann method is given next.

A general lattice Boltzmann method consists of three important parts: namely the evolution equation of distribution function, equilibrium distribution function and the lattice. Discrete Boltzmann equation and discrete passive-scalar equation are used as the evolution equation of density distribution function and temperature distribution function, respectively. $f_i(\vec{x}, t)$ and $g_i(\vec{x}, t)$ are density distribution function and temperature distribution function at point $\vec{x}$ and time t respectively, they can be calculated as follows:

$$f_i(\vec{x} + \vec{e}_i\delta_t, t + \delta_t) - f_i(\vec{x}, t) = -\frac{1}{\tau}(f_i(\vec{x}, t) - f_i^{eq}(\vec{x}, t)) + \Delta f_i(\vec{x}, t) \tag{1}$$

$$g_i(\vec{x} + \vec{e}_i\delta_t, t + \delta_t) - g_i(\vec{x}, t) = -\frac{1}{\tau_T}(g_i(\vec{x}, t) - g_i^{eq}(\vec{x}, t)) + \delta_t\omega_i\Phi \tag{2}$$

$$f_i^{eq} = \omega_i\rho\left[1 + \frac{\vec{e}_i\cdot\vec{u}}{c_s^2} + \frac{(\vec{e}_i\cdot\vec{u})^2}{2c_s^4} - \frac{\vec{u}^2}{2c_s^2}\right] \tag{3}$$

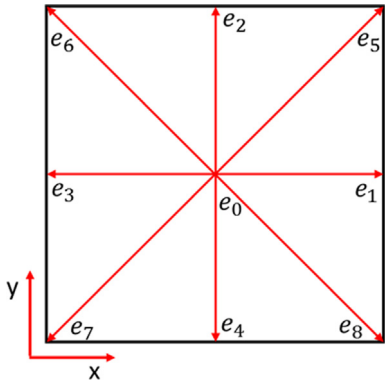

Fig. 1. D2Q9.

$$g_i^{eq} = \omega_i T\left[1 + \frac{\vec{e}_i\cdot\vec{U}}{c_s^2} + \frac{(\vec{e}_i\cdot\vec{U})^2}{2c_s^4} - \frac{\vec{U}^2}{2c_s^2}\right] \tag{4}$$

f_i^{eq} and g_i^{eq} are equilibrium density distribution function and equilibrium temperature distribution, respectively. The evolution equation of density distribution function is obtained by the discrete of Boltzmann-BGK equation. The evolution equation of temperature distribution is obtained by the following passive-scalar equation, in which the viscous heat dissipation is neglected:

$$\frac{\partial T}{\partial t} + \nabla\cdot(\boldsymbol{U}T) = \nabla\cdot(\alpha\nabla T) + \Phi \tag{5}$$

D2Q9 lattice is used for our simulation, as shown in Fig. 1, which has nine velocities in one lattice site in a two-degree space. $\vec{e}_i$ ($i = 0, 8$ for D2Q9 lattice) is the discrete speed in i-th direction. ω_i is the weighting coefficient. τ and τ_T are the relaxation time of density distribution function and temperature distribution function respectively. c_s is the lattice sound speed. $\vec{u}$ is the velocity, but the real velocity of the fluid is $\vec{U}$.

For D2Q9 lattice, it has:

$$\vec{e}_i = \begin{cases} (0, 0), & i = 0 \\ (\pm1, 0)c,\ (0, \pm1)c & i = 1, 4 \\ (\pm1, \pm1)c & i = 5, 8 \end{cases} \tag{6}$$

$$\omega_i = \begin{cases} 4/9, & i = 0 \\ 1/9, & i = 1, 4 \\ 1/36, & i = 5, 8 \end{cases} \tag{7}$$

where $c = \delta_x/\delta_t$ is the lattice speed. δ_x is one lattice length unit, and δ_t is one timestep in lattice unit. δ_x and δ_t are usually taken to be 1.0 for simplicity. Lattice sound speed $c_s = c^2/3$. The kinematic viscosity and thermal diffusivity are given by:

$$\upsilon = c_s^2\left(\tau - \frac{1}{2}\right)\delta_t \tag{8}$$

$$\alpha = c_s^2\left(\tau_T - \frac{1}{2}\right)\delta_t \tag{9}$$

Exact difference method(EDM) was proposed by Kupershtokh and Medveden [33], and we adopt this method to incorporate force in LBM. In this way, the force is directly added to the right-hand side of Eq. (1), so the force term can be written as:

$$\Delta f_i(\vec{x}, t) = f_i^{eq}(\rho(\vec{x}, t), \vec{u} + \Delta\vec{u}) - f_i^{eq}(\rho(\vec{x}, t), \vec{u}) \tag{10}$$

For the evolution function of temperature, Φ is the source term that responsible for phase change. The derivation of Φ one can refer to [34]:

$$\Phi = T\left[1 - \frac{1}{\rho c_v}\left(\frac{\partial P}{\partial T}\right)_\rho\right]\nabla\cdot\vec{U} \tag{11}$$

After every collision-diffusion time-step, we can obtain density ρ, velocity $\vec{U}$ and temperature T of every lattice:

$$\rho = \sum_i f_i \tag{12}$$

$$\rho\vec{u} = \sum_i \vec{e}_i f_i \tag{13}$$

$$\rho\vec{U} = \sum_i \vec{e}_i f_i + \frac{\delta_t}{2}\vec{F} \tag{14}$$

$$\mathrm{T} = \sum_i g_i \tag{15}$$

where $\vec{F}$ is the force of fluid. In our simulation, the force $\vec{F}$ is composed of three different portions, namely fluid-fluid interaction $\vec{F}_{int}$, fluid-solid interaction $\vec{F}_s$, and gravity $\vec{F}_g$:

$$\vec{F} = \vec{F}_{int} + \vec{F}_s + \vec{F}_g \tag{16}$$

for the interaction of fluid and fluid, we adopt Shan-Chen pseudo-potential model for introducing a nonlocal interaction [35]:

$$\vec{F}_{int}(\vec{x}) = -c_0\Psi(\vec{x})g\nabla\Psi(\vec{x}) \tag{17}$$

and Gong has proposed a discrete form for its numerical implementation [36]:

$$\vec{F}_{int}(\vec{x}) = -\beta\Psi(\vec{x})\sum_{\vec{x}} G(\vec{x},\vec{x}')\Psi(\vec{x}')(\vec{x}-\vec{x}') - \frac{1-\beta}{2}\sum_{\vec{x}'} G(\vec{x},\vec{x}')\Psi(\vec{x}')^2(\vec{x}-\vec{x}') \tag{18}$$

β is an adjustable constant for numerical accuracy, $G(\vec{x},\vec{x}')$ is the Green function which measures the strength of interactions. For D2Q9 lattice, it can be given:

$$G(\vec{x},\vec{x}') = \begin{cases} 2g, & |\vec{x}-\vec{x}'| = 1 \\ g/2, & |\vec{x}-\vec{x}'| = \sqrt{2} \\ 0, & otherwise \end{cases} \tag{19}$$

where g is a constant. As shown in Eq. (14), only interactions on neighboring lattices are taken into account in the simulation. $\Psi(\vec{x})$ is the "effective mass" which is a function of the local density and control the detailed nature of the interaction potential, and it depends on the equation of state of the system:

$$\Psi(\rho) = \sqrt{\frac{2(p-\rho c_s^2)}{c_0 g}} \tag{20}$$

In order to get a more accurate simulation for real gases, we choose Peng-Robinson (P-R) equation of state:

$$\mathrm{p} = \frac{\rho RT}{1-b\rho} - \frac{a\rho^2 \in (T)}{1+2b\rho-b^2\rho^2} \tag{21}$$

where $\in(T) = [1+(0.37464+1.54226\omega-0.26992\omega^2)(1-\sqrt{T/T_c})]^2$, with ω being the acentric factor that is relevant to the working fluid. For the water that we utilized as working fluid in our following simulation, ω is chosen as 0.344. "a" and "b" are arbitrary constants but should be carefully selected for proper critical properties p_c, ρ_c and T_c. Because the first and second derivatives of p to ρ are set to zero, we can get $\mathrm{a} = 0.45724R^2T_c^2/p_c$ and $\mathrm{b} = 0.0778\mathrm{R}T_c/p_c$.

Fluid-solid interaction and body force gravity have the following form for D2Q9 scheme [37]:

$$\vec{F}_s(\vec{x}) = -\Psi(\vec{x})\sum_i g_s\omega_i s(\vec{x}+\vec{e}_i\delta_t)\cdot\vec{e}_i\delta_t \tag{22}$$

$$\vec{F}_g(\vec{x}) = g_0\cdot(\rho(\vec{x})-\rho_{ave}) \tag{23}$$

with g_s being constant for adjusting the strength of fluid-solid interaction. g_0 is the acceleration of gravity, and ρ_{ave} is the average density of all lattices. $s(\vec{x})$ is an indication of 1 and 0 for solid particle and fluid particle.

Utilized the above lattice Boltzmann method, we write the program with Fortran language under Linux operating system and the GNU

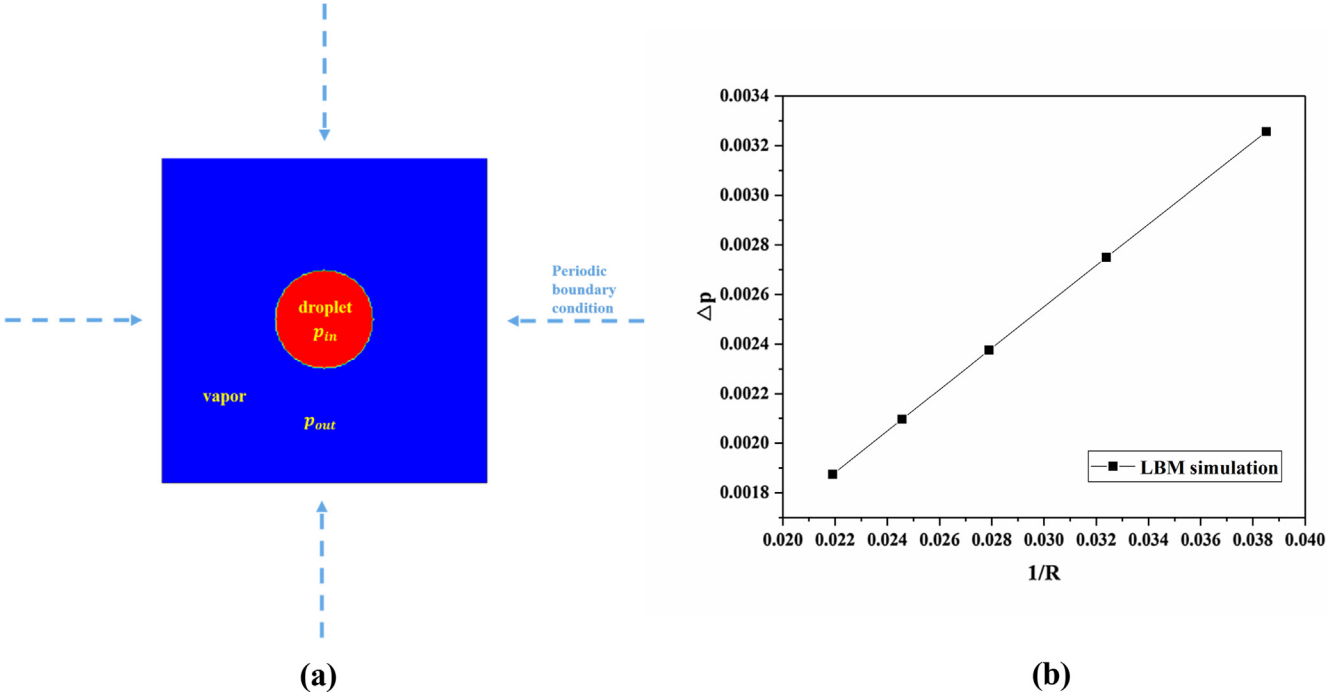

Fig. 2. Laplace's law validation.

compiler collection is used. All the simulations are done on a workstation with two 6-core CPUs (E5-2620 v2) and 64 GB RAM.

3. Simulation and results

3.1. Model verification

3.1.1. Laplace's law verification

Laplace's law can be written as

$$\Delta p = p_{in} - p_{out} = \frac{\sigma}{R} \tag{24}$$

at the initial time, a droplet with radial R_0 suspended in it's vapor, the whole computation domain is set 200 * 200. It is worth to be noted that, all the units in our simulation are in the lattice units and the lattice units can be transformed to the physical units by some dimensionless numbers. As Fig. 2(a) shows, the periodic boundary conditions are applied on the boundary, and the vapor and droplet are in saturation temperature of 0.9 * Tc (Tc is the critical temperature). The simulation results are showed in the Fig. 2(b). It should be noted that the droplet radial R is selected when the simulation is in the steady state, but not the R_0 that set at the initial time, although R is almost equal to R_0. It can be seen from Fig. 2(b) that the results are corresponding to Laplace's law and the surface tension is $\sigma = 0.08322$ by linearly fitting.

3.1.2. d^2 law verification

Droplet evaporation simulation is always used for model validation in the LBM simulation. In this part, d^2 law for droplet evaporation is used for a phase change model verification, which indicates that the square of the droplet diameter changes linearly with time. At the initial time, a droplet with diameter $D_0 = 120$ suspends in the central of 300 * 300 lattices domain and the rest of the domain is full of vapor. The initial temperature of the droplet is set 0.9 * Tc, and the droplet is in a saturation state. In order to verify the d^2 law, the superheat temperature of the vapor is set 0.04 * Tc and 0.08 * Tc respectively. The viscous heat dissipation and the buoyancy are not considered in the simulation. Periodic boundary conditions are applied in all boundaries, as Fig. 3(a) shows. The results are given in the Fig. 3(b). These results show that the square of the droplet diameter changes linearly with time step and higher temperature corresponds to a faster evaporation rate. These results are corresponding to the d^2 law, so our model is reliable for the liquid-vapor phase change simulation.

3.2. Nuclear boiling in different shapes of gasification core surface

The research about the effects of cavity geometry on nuclear boiling is very limited. For one hand, it's hard to only consider the cavity geometry effects in the experiment, for another hand, it is not easy to process a series of different cavity geometry surfaces for the experiment. Because of the complexity of boiling heat transfer, theoretical study about the cavity geometry is also deficient. In this paper, we will use LBM to simulate sole nucleate site boiling heat transfer on four different cavity geometry surfaces, which are square, circular, trapezoidal, and inverted trapezoidal surfaces.

Lattice Boltzmann method is used to simulate sole nucleate site boiling heat transfer on four different cavity geometry surfaces, these four surfaces are displayed in Fig. 4. In our simulation, constant temperature boundary condition is applied in the solid bottom, and for the horizontal direction, periodic boundary condition is adopted. In the initial time, the liquid is in the saturation condition at the temperature of 0.9 * Tc and the constant temperature in the solid bottom is sat 0.96 * Tc, which can guarantee a nucleate boiling in the liquid-solid surface. The whole computation domain size is L x× $Ly = 200 \times 700$ lattice, and the height of the solid is 100 lattice. For more information about the lattice size, one can view the reference [30]. By the Maxwell construction, the densities of the saturation liquid and vapor can be obtained, which are $\rho_l = 5.9$ and $\rho_v = 0.58$. The physical quantities that used for liquid are: specific heat capacity $c_{p.l} = c_{v,l} = 4.0$, the dynamic viscosity $\mu_l = 0.354$, the thermal diffusivity $\alpha_l = 0.05$. The physical quantities that used for vapor are: specific heat capacity $c_{p,v} = c_{v,v} = 2.0$, the dynamic viscosity $\mu_v = 0.1025$, the thermal diffusivity $\alpha_v = 0.0867$. So the Prandtl number can be obtained that $P_{rl} = 1.2$ and $P_{rv} = 2.038$. The physical quantities that used for vapor are: $(\rho c_p)_s = 23.6$, the thermal diffusivity $\alpha_s = 4$. The viscous thermal dissipation is neglected in the simulation. The gravity and contact angle also have important effects on the boiling phenomenon, so in this simulation, the gravity is set $g = 0.0003$ and $g_s = -0.2$. Utilizing the conjugate heat transfer method that Li et al. posted for the fluid-solid interface, the temperature

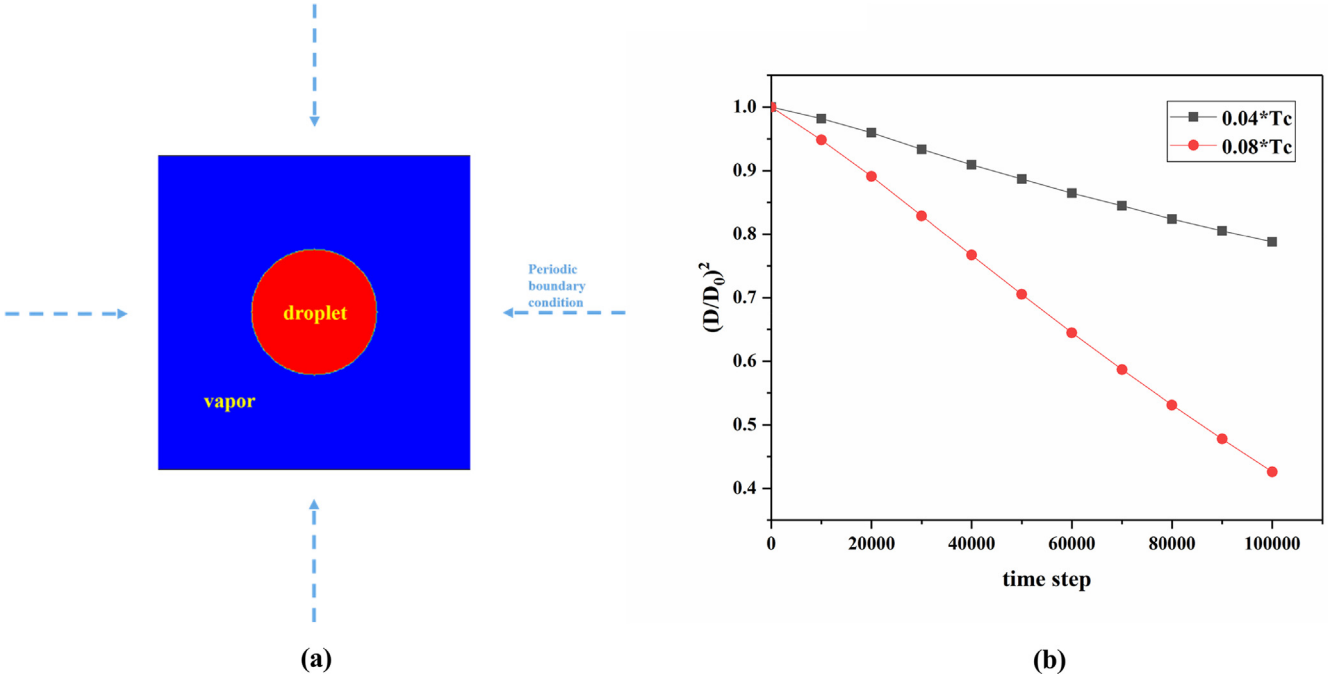

Fig. 3. d^2 law validation.

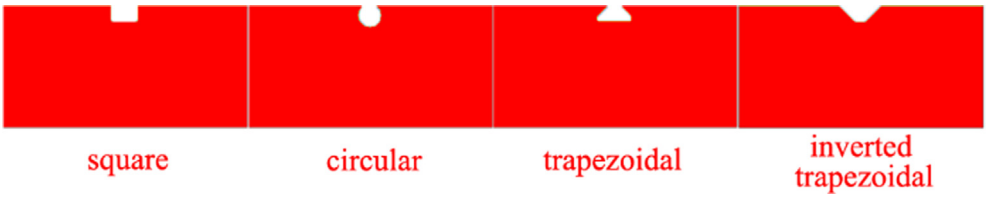

Fig. 4. Four different cavity geometry surfaces.

distribution function at the fluid-solid interface can be written as [38]:

$$g_{i^-}(\vec{x}_f, t+\delta_t) = \frac{1-\gamma}{1+\gamma}\widehat{g_i}(\vec{x}_f, t) + \frac{2\gamma}{1+\gamma}\widehat{g_{i^-}}(\vec{x}_s, t) \tag{25}$$

$$g_i(\vec{x}_s, t+\delta_t) = -\frac{1-\gamma}{1+\gamma}\widehat{g_{i^-}}(\vec{x}_s, t) + \frac{2}{1+\gamma}\widehat{g_i}(\vec{x}_f, t) \tag{26}$$

where γ is defined as $\gamma = (\rho c_p)_s/(\rho c_p)_f$, it means the thermal mass ratio of the solid and the fluid.

Fig. 5(a) gives some pictures about the first bubble nucleate, growth and departure from four different surfaces. As a whole, nucleate boiling occurs on all surfaces in the given superheat temperature, but different cavity geometry surface has different onset boiling time and onset boiling temperature distribution. In the hydrophilic surface used in our simulation, square and inverted trapezoidal cavity geometry surfaces can be put in the same class as these two surfaces have almost the same onset boiling time and onset boiling temperature distribution. The rest two surfaces, which means circular and trapezoidal cavity geometry surfaces, are also put in the same class as the same reason. It can be found from Fig. 5(a) that, bubble growth process can be divided into two periods: when the bubble is small, surface tension is dominant, so in this period, bubble will grow bigger and bigger but the shape doesn't change; for the second period, buoyancy is dominant, so bubble continues to grow but tensile deformation will occur for the bubble shape, and this tensile deformation will last until bubble departures from the surface.

For the first class with square and inverted trapezoidal cavity geometry surfaces, the onset nucleate boiling time is 13,800 time step, which is late than the second class 6800 time step. In order to explain this difference, Fig. 5(b) gives the corresponding temperature distribution pictures. The first class temperature distribution pictures show that, there is more uniform temperature distribution in the solid-liquid surface at the onset nucleate boiling time, but for the second class, when the phase change takes place, the temperature in the cavity is higher a lot than the temperature in the solid-liquid surface. These results show that for the first class surfaces, there are bigger cavities opening, so it's hard to form a high temperature core in the cavities, in this condition, liquid begins to evaporate in a more uniform temperature distribution; but for the second class surfaces, which have smaller cavities opening, it is easy to form a high temperature core in the cavities, so in this condition, onset nucleate boiling time is shorter than the first class surfaces.

Heat flux is also computed in our simulation. Referring to Fourier's law of heat conduction, in the discrete form, heat flux in the x, y, z direction can be expressed as:

$$q_x = -k\frac{T(x+\Delta x, y, z) - T(x, y, z)}{\Delta x}$$

$$q_y = -k\frac{T(x, y+\Delta y, z) - T(x, y, z)}{\Delta y}$$

$$q_z = -k\frac{T(x, y, z+\Delta z) - T(x, y, z)}{\Delta z}$$

so the total heat flux q can be written as:

$$q = \sqrt{q_x^2 + q_y^2 + q_z^2} \tag{27}$$

Consulting to Eq. (24), average heat flux variation with the time step in the solid-liquid surface is showed in Fig. 6. The heat flux curves have also obviously divided into two categories, as mentioned before, the heat flux in square cavity surface and inverted trapezoidal cavity surface have the same trend, and other two surfaces also have the same trend. Fig. 6(a) is the heat flux variation picture before 150,000 time step. Nearly after 30,000 time step, the heat flux in the four surfaces show periodic fluctuations, corresponding to the bubble periodic growth and departure from the surfaces. Because the constant temperature boundary condition is applied in the solid bottom, with the liquid temperature going up, the heat flux between the solid-liquid surface will go down, so the heat flux show a downtrend in general in Fig. 6(a). In order to detail the different phenomenon of the four surfaces, Fig. 6(b)–(d) give the heat flux variation pictures before 25,000 time step. It can be found in Fig. 6(b) that circular and trapezoidal surfaces have the same trend and square and inverted trapezoidal surfaces have another same trend, and before 1200 time step, the heat flux shows a sharp rise in the four different surfaces. This sharp rise is caused by a faster solid thermal conductivity compared with liquid thermal conductivity, so the temperature difference gradually increases in the solid-liquid interface until attaining to a stable temperature distribution in the solid. For a convenient description, average interface heat flux variation with time step pictures in circular surface and square surface are given alone for Fig. 6(c) and (d). In Fig. 6(c) and (d), we marked some special time step for a bubble nucleate and growth in a cavity. For Fig. 6(c), about at the 5800 time step, the liquid begin to gasification in the circular cavity. With the gasification taking place, the heat flux will go up in a period of time because of the heat of vaporization. About at the 8600 time step, when the vapor covers the cavity, the heat flux will go down. But this downtrend will not last for a long time, nearly at the 9600 time step, buoyancy is dominant, although bubble continues to grow tensile deformation will occur for the bubble shape. In this condition, the heat flux will go up and this tensile deformation will last until bubble departures from the surface. Fig. 6(d) nearly has the same trend with (c), except that square cavity surface has longer waiting time for the first bubble nucleation.

In order to give a clear explanation for the mechanism of nucleate boiling heat transfer, Fig. 7 gives the heat flux variation with the position and time step in the liquid-solid interface. It can be found that the highest heat flux takes place near the cavity exit, and it's value nearly 10 times to the other positions, except that in the inverted trapezoidal cavity surface, which has the biggest aperture radius. In the medium of the surface, corresponding to x = 100, is the vapor cavity, so the heat flux is lowest. In addition, because of a shorter onset nucleate time for the circular and trapezoidal cavity surfaces, the liquid temperatures relatively lower than it in the square and inverted trapezoidal cavity surfaces, so the heat fluxes are bigger in the circular and trapezoidal cavity surfaces at the positions except the cavity. The heat flux at the cavity exit on the inverted trapezoidal surface is obviously lower than on the other three surfaces. This result shows that increasing width cavity (from inside to the outside) has the worst heat transfer performance in comparable to the other surfaces, which include decreasing width cavity (trapezoidal), first increasing then decreasing width cavity (circular) and maintaining width cavity (square). The decreasing width cavity surfaces, no matter for the trapezoidal or the circular cavity surfaces, have the best heat transfer performances.

Consulting to Fig. 6(c) and (d) can be found that at the 10,800 time step on the circular cavity surface and 19,200 time step on the square

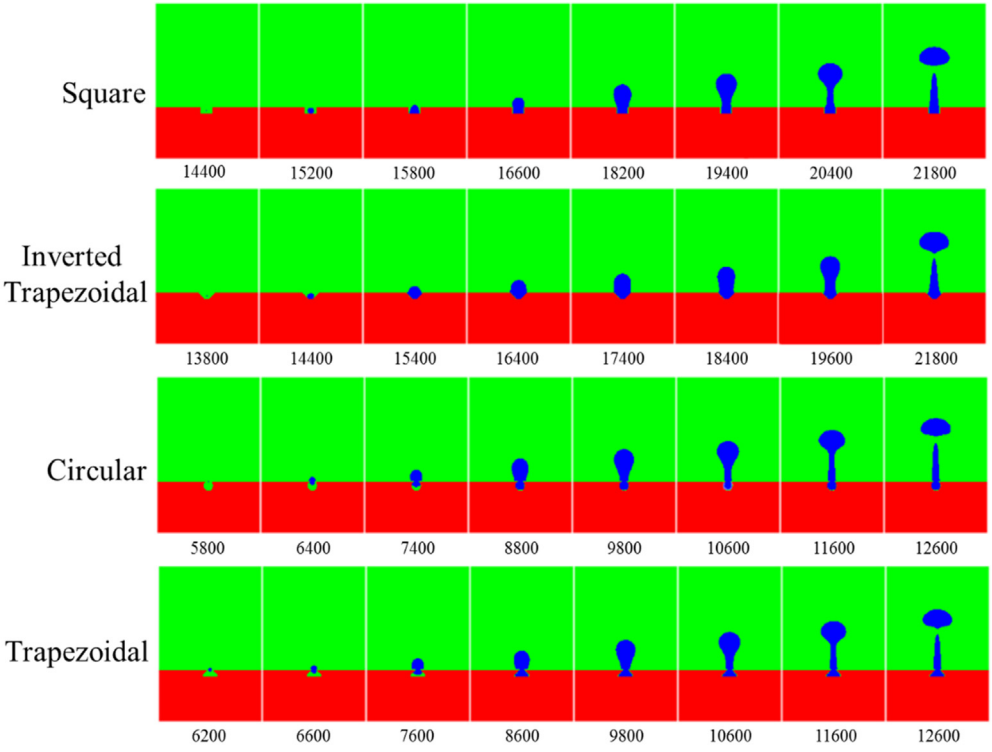

(a)

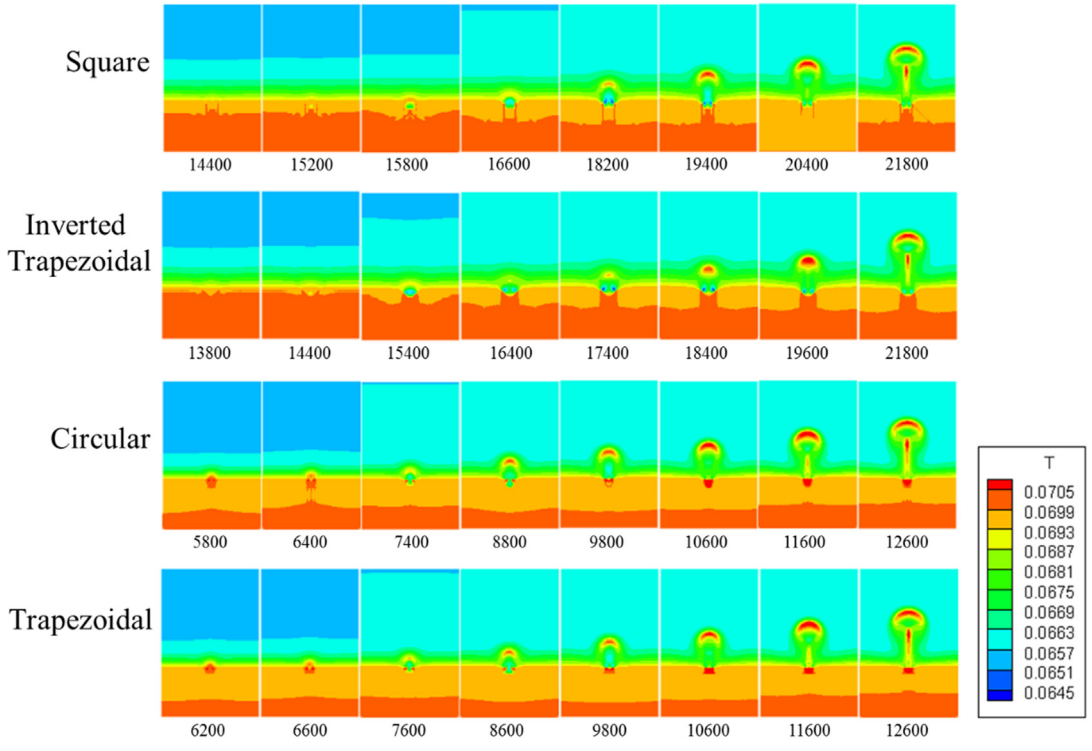

(b)

Fig. 5. The first bubble nucleate, growth, and departure from the four surfaces. (a) Density distribution; (b) Temperature distribution.

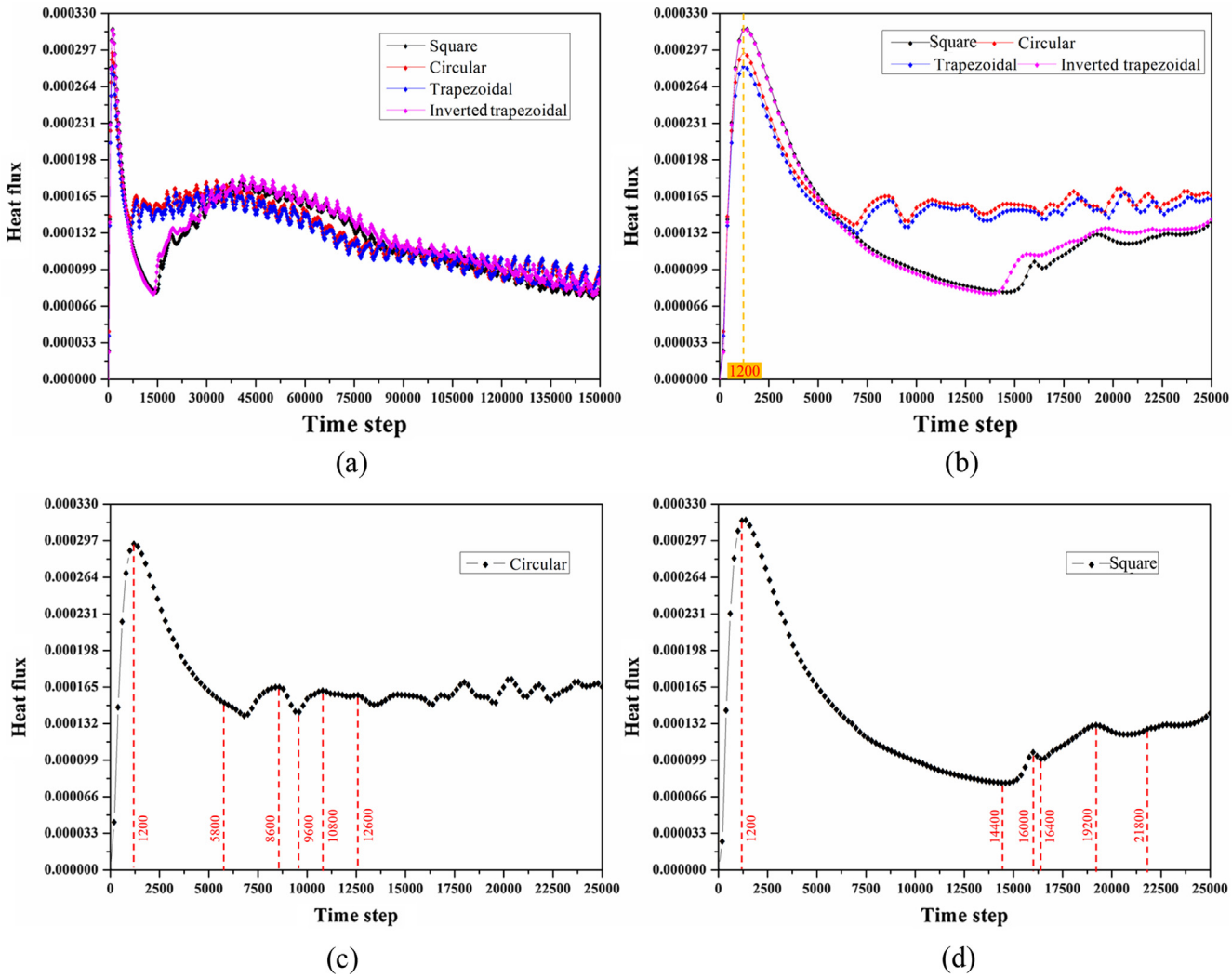

Fig. 6. Average heat flux variation in vapor-liquid interface.

cavity surface are the time when the heat fluxes come to highest because of bubble tensile deformation. Fig. 8 gives the density distribution, temperature distribution and heat flux distribution pictures at 19,200 time step on the square cavity surface and 10,800 time step on circular cavity surface. For the density distribution pictures, the bubble necks occur on the effect of tensile deformation on these two surfaces. But the temperature distribution pictures are obviously different. For the square cavity surface, there is more uniform temperature distribution in the solid-liquid surface at the onset nucleate boiling time, but for the circular cavity surface, when the phase change takes place, the temperature in the cavity is higher a lot than the temperature in the solid-liquid surface. So when the bubble growth, because of the absorption of heat, the former class surfaces show a lower temperature but the latter class surfaces still have a higher temperature in the cavity. By analyzing the heat flux distribution pictures, it is obvious to found that on the process of bubble growth, the mainly heat transfer occurred in the bubble liquid interface and microlayer evaporation. The highest heat flux occurs in the cavity export that is leaded by the microlayer evaporation. So we think the main heat transfer mechanism is the microlayer evaporation in the nuclear boiling.

4. Conclusion

In this paper, pseudo-potential liquid-vapor phase change lattice Boltzmann method is used to simulate nucleate boiling on the surfaces with four different geometry cavities, which is square cavity surface, circular cavity surface, trapezoidal cavity surface and inverted trapezoidal cavity. Bubble growth on different surfaces and corresponding heat flux variation in the liquid-solid surface are showed in this paper. Some conclusions can be abstracted from this paper:

1. Different surface has different onset boiling time, and this onset boiling time is mainly effected by the opening radius of the cavity on the same superheat temperature. In our simulation, circular cavity surface and trapezoidal cavity surface have nearly the same onset boiling time 6000 time step, where square and inverted trapezoidal cavity surface nearly 14,000 time step. In addition, results show that increasing width cavity (from inside to the outside) has the worst heat transfer performance in comparable to the other surfaces, which include decreasing width cavity (trapezoidal), first increasing then decreasing width cavity (circular) and maintaining width cavity (square). The decreasing width cavity surfaces, no matter for the trapezoidal or the circular cavity surfaces, have the best heat transfer performances.
2. The temperature distribution for the first bubble nucleation has obvious difference on square, inverted trapezoidal cavity surfaces and on circular, trapezoidal cavity surfaces. For the square and inverted trapezoidal cavity surfaces, which is classified to the first class, there is more uniform temperature distribution in the solid-liquid surface at the onset nucleate boiling time, but for the circular

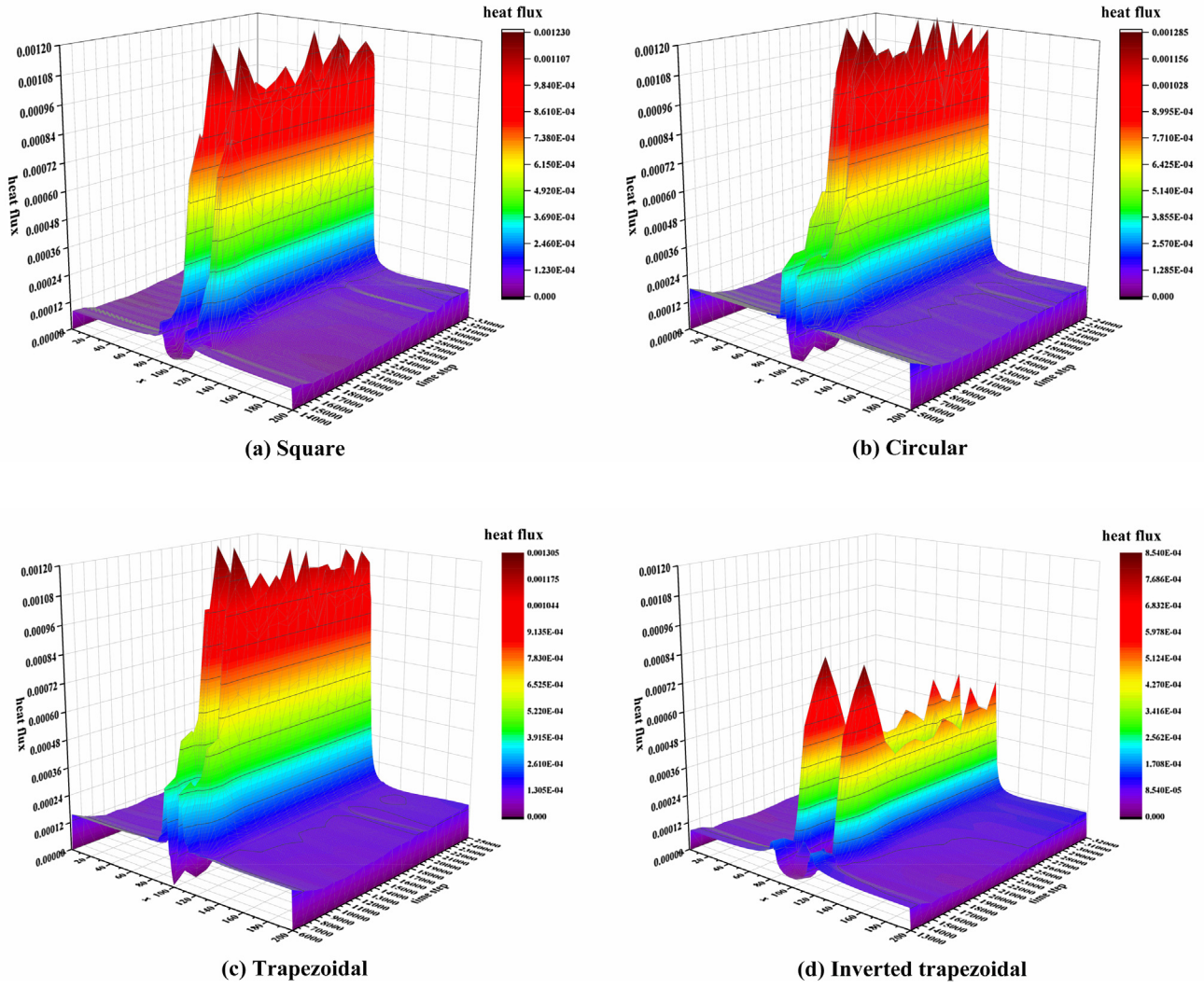

Fig. 7. Heat flux variation in liquid-solid interface.

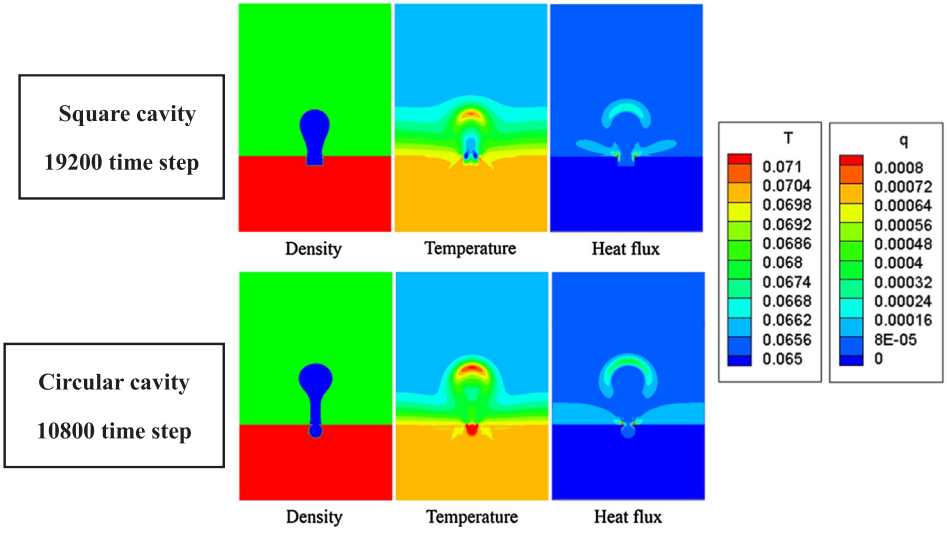

Fig. 8. Density distribution, temperature distribution and heat flux distribution.

and trapezoidal cavity surfaces, which is classified to the second class, when the phase change takes place, the temperature in the cavity is higher a lot than the temperature in the solid-liquid surface. So when the bubble growth, because of the absorption of heat, the former class surfaces show a lower temperature but the latter class surfaces still have a higher temperature in the cavity.

3. Liquid-solid interface average heat flux variation is analyzed corresponding to the bubble growth process. It indicates that when the bubble begins to nucleate, the heat flux goes up until the cavity is filled with vapor. Then the heat flux will go down until the buoyancy is dominant, and tensile deformation occurs to the bubble.
4. By analyzing the heat flux distribution pictures, it is obvious to found that on the process of bubble growth, the mainly heat transfer occurred in the bubble liquid interface and microlayer evaporation. The highest heat flux occurs in the cavity export that is leaded by the microlayer evaporation. So we think the main heat transfer mechanism is the microlayer evaporation in the nuclear boiling.

Acknowledgment

The work is supported by the National Natural Science Foundation of China (NOs. 51776079 & 51736004) and the National Key Research and Development Program of China (NO. 2017YFB0603501-3).

References

[1] V.K. Dhir, Boiling heat transfer, Annu. Rev. Fluid Mech. 30 (1998) 365–401.
[2] V.K. Dhir, G.R. Warrier, E. Aktinol, Numerical simulation of pool boiling: a review, J. Heat Transf. – Trans. ASME 135 (6) (2013) 17.
[3] N. Zuber, Hydrodynamic aspects of boiling heat transfer(phd), 1959.
[4] M. Jakob, Heat Transfer in Evaporation and Condensation, University of Illinois, 1937.
[5] J. Kim, Review of nucleate pool boiling bubble heat transfer mechanisms, Int. J. Multiphase Flow 35 (12) (2009) 1067–1076.
[6] B.B. Mikic, W.M. Rohsenow, A new correlation of pool-boiling data including the effect of heating surface characteristics, J. Heat Transfer 91 (2) (1969) 245–250.
[7] P. Stephan, J. Hammer, A new model for nucleate boiling heat transfer, Heat Mass Transfer 30 (2) (1994) 119–125.
[8] P. Deng, Y.-K. Lee, P. Cheng, An experimental study of heater size effect on micro bubble generation, Int. J. Heat Mass Transfer 49 (15) (2006) 2535–2544.
[9] D.M. Qiu, V.K. Dhir, D. Chao, M.M. Hasan, E. Neumann, G. Yee, A. Birchenough, Single-bubble dynamics during pool boiling under low gravity conditions, J. Thermophys. Heat Transfer 16 (3) (2002) 336–345.
[10] M. Buchholz, H. Auracher, T. Lüttich, W. Marquardt, A study of local heat transfer mechanisms along the entire boiling curve by means of microsensors, Int. J. Therm. Sci. 45 (3) (2006) 269–283.
[11] S.J. Thiagarajan, R. Yang, C. King, S. Narumanchi, Bubble dynamics and nucleate pool boiling heat transfer on microporous copper surfaces, Int. J. Heat Mass Transfer 89 (2015) 1297–1315.
[12] Y. Diao, Y. Zhao, Q. Wang, Visualization of bubble dynamics for pool boiling of binary refrigerant mixture R11–r11311 supported by the national natural science foundation of China (No.10355001) and the century programme of Chinese academy of sciences, Chinese J. Chem. Eng. 14 (2) (2006) 149–157.
[13] Y.H. Zhao, Y.H. Diao, T. Takaharu, Experimental investigation in nucleate pool boiling of binary refrigerant mixtures, Appl. Therm. Eng. 28 (2) (2008) 110–115.
[14] A. Abdollahi, M.R. Salimpour, N. Etesami, Experimental analysis of magnetic field effect on the pool boiling heat transfer of a ferrofluid, Appl. Therm. Eng. 111 (2017) 1101–1110.
[15] S. Hariri, M. Mokhtari, M.B. Gerdroodbary, K. Fallah, Numerical investigation of the heat transfer of a ferrofluid inside a tube in the presence of a non-uniform magnetic field, Europ. Phys. J. Plus 132 (2) (2017) 65.
[16] D. Ciloglu, A. Bolukbasi, A comprehensive review on pool boiling of nanofluids, Appl. Therm. Eng. 84 (2015) 45–63.
[17] R. Kamatchi, S. Venkatachalapathy, Parametric study of pool boiling heat transfer with nanofluids for the enhancement of critical heat flux: a review, Int. J. Therm. Sci. 87 (2015) 228–240.
[18] S. Mori, Y. Utaka, Critical heat flux enhancement by surface modification in a saturated pool boiling: a review, Int. J. Heat Mass Transfer 108 (2017) 2534–2557.
[19] S. Mori, S. Mt Aznam, K. Okuyama, Enhancement of the critical heat flux in saturated pool boiling of water by nanoparticle-coating and a honeycomb porous plate, Int. J. Heat and Mass Transfer 80 (2015) 1–6.
[20] S. Launay, A. Fedorov, Y. Joshi, A. Cao, P. Ajayan, Hybrid micro-nano structured thermal interfaces for pool boiling heat transfer enhancement, Microelectron. J. 37 (11) (2006) 1158–1164.
[21] L. Dong, X. Quan, P. Cheng, An experimental investigation of enhanced pool boiling heat transfer from surfaces with micro/nano-structures, Int. J. Heat Mass Transfer 71 (2014) 189–196.
[22] K.-H. Chu, R. Enright, E.N. Wang, Structured surfaces for enhanced pool boiling heat transfer, Appl. Phys. Lett. 100 (24) (2012) 241603.
[23] Y. Tang, B. Tang, Q. Li, J. Qing, L. Lu, K. Chen, Pool-boiling enhancement by novel metallic nanoporous surface, Exp. Therm. Fluid Sci. 44 (2013) 194–198.
[24] D. Saeidi, A. Alemrajabi, Experimental investigation of pool boiling heat transfer and critical heat flux of nanostructured surfaces, Int. J. Heat Mass Transfer 60 (2013) 440–449.
[25] S. Ryu, S. Ko, Direct numerical simulation of nucleate pool boiling using a two-dimensional lattice Boltzmann method, Nucl. Eng. Des. 248 (2012) 248–262.
[26] T. Sun, W. Li, S. Yang, Numerical simulation of bubble growth and departure during flow boiling period by lattice Boltzmann method, Int. J. Heat Fluid Flow 44 (2013) 120–129.
[27] A. Begmohammadi, M. Farhadzadeh, M.H. Rahimian, Simulation of pool boiling and periodic bubble release at high density ratio using lattice Boltzmann method, Int. Commun. Heat Mass Transfer 61 (2015) 78–87.
[28] R. Sadeghi, M.S. Shadloo, M.Y.A. Jamalabadi, A. Karimipour, A three-dimensional lattice Boltzmann model for numerical investigation of bubble growth in pool boiling, Int. Commun. Heat Mass Transfer 79 (2016) 58–66.
[29] Q. Li, Q.J. Kang, M.M. Francois, Y.L. He, K.H. Luo, Lattice Boltzmann modeling of boiling heat transfer: the boiling curve and the effects of wettability, Int. J. Heat Mass Transfer 85 (2015) 787–796.
[30] S. Gong, P. Cheng, Direct numerical simulations of pool boiling curves including heater's thermal responses and the effect of vapor phase's thermal conductivity, Int. Commun. Heat Mass Transfer 87 (2017) 61–71.
[31] W.-Z. Fang, L. Chen, Q.-J. Kang, W.-Q. Tao, Lattice Boltzmann modeling of pool boiling with large liquid-gas density ratio, Int. J. Therm. Sci. 114 (2017) 172–183.
[32] S. Gong, P. Cheng, A lattice Boltzmann method for simulation of liquid–vapor phase-change heat transfer, Int. J. Heat Mass Transfer 55 (17–18) (2012) 4923–4927.
[33] A. Kupershtokh, D. Medvedev, Lattice Boltzmann equation method in electrohydrodynamic problems, J. Electrostat. 64 (7) (2006) 581–585.
[34] S. Gong, P. Cheng, Lattice Boltzmann simulation of periodic bubble nucleation, growth and departure from a heated surface in pool boiling, Int. J. Heat Mass Transfer 64 (2013) 122–132.
[35] X. Shan, H. Chen, Lattice Boltzmann model for simulating flows with multiple phases and components, Phys. Rev. E 47 (3) (1993) 1815–1819.
[36] S. Gong, P. Cheng, Numerical investigation of droplet motion and coalescence by an improved lattice Boltzmann model for phase transitions and multiphase flows, Comput. Fluids 53 (2012) 93–104.
[37] N.S. Martys, H. Chen, Simulation of multicomponent fluids in complex three-dimensional geometries by the lattice Boltzmann method, Phys. Rev. E 53 (1) (1996) 743–750.
[38] L. Li, C. Chen, R. Mei, J.F. Klausner, Conjugate heat and mass transfer in the lattice Boltzmann equation method, Phys. Rev. E 89 (4) (2014) 043308.